Direct numerical simulation of laminar and turbulent Bénard convection

By GÜNTHER GRÖTZBACH

Institut für Reaktorentwicklung, Kernforschungszentrum Karlsruhe,
Postfach 3640, D-7500 Karlsruhe, Federal Republic of Germany

The TURBIT-3 computer code has been used for the direct numerical simulation of Bénard convection in an infinite plane channel filled with air. The method is based on the three-dimensional non-steady-state equations for the conservation of mass, momentum and enthalpy. Subgrid-scale models of turbulence are not required, as calculations with different grids show that the spatial resolution of grids with about $32^2 \times 16$ nodes provides sufficient accuracy for Rayleigh numbers up to $Ra = 3 \cdot 8 \times 10^5$. Hence this simulation model contains no tuning parameters.

The simulations start from nearly random initial conditions. This has been found to be essential for calculating flow patterns and statistical data insensitive to grid parameters and agreeing with experimental experience. The numerical results show the theoretically predicted 'skewed varicose' instability at $Ra = 4000$. Warm and cold 'blobs' are identified as causing temperature-gradient reversals for all the high Rayleigh numbers under consideration. The calculated wavelengths and the corresponding flow regimes observed in the transition range confirm the stability maps determined theoretically. In the turbulent range the wavelengths agree qualitatively with low-aspect-ratio experiments. Accordingly, the Nusselt numbers lie at the upper end of the scatter band of experimental data, as these also depend on the aspect ratio. Appropriately normalized, the velocity and temperature fluctuation peaks are independent of the Rayleigh number. The vertical profiles agree largely with experimental data and, especially in case of temperature statistics, exhibit comparable or less scatter.

1. Introduction

In this paper the classical Bénard problem of thermal convection in a horizontal infinite fluid layer heated uniformly from below is investigated by direct numerical simulation. The method is based on the solution of the complete, non-steady-state, three-dimensional equations of the conservation of mass, momentum and heat. The gross structure of the turbulent fields is described directly by a finite-difference grid. If grids with poor resolution are used, subgrid-scale structure models are necessary to describe the exchanges of momentum and heat of the small turbulence elements not resolved by the grid.

Although direct numerical simulation has already been applied to a few cases of Bénard convection, it has not yet been applied to the investigation of turbulent convection at high Rayleigh numbers. Earlier work, as presented by Deardorff & Willis (1965) and Lipps & Somerville (1971), is based on a two-dimensional formulation of

the fundamental equations without the use of a subgrid-scale model. The two-dimensional simulations run into various problems, for example the computed heat transfer is too high, and the transition from laminar to turbulent flow is calculated to occur at Rayleigh numbers higher than those observed experimentally (Deardorff & Willis 1965). In the three-dimensional simulations by Lipps & Somerville (1971) and Ozoe *et al.* (1976) no subgrid-scale models were used; instead, simulations were carried out mainly for laminar and transition flow regimes. For turbulent convection only one simulation case is known for $Ra = 25\,000$ (Lipps 1976). The problems stated are the strong influences of the grid widths chosen and of the periodicity lengths on the calculated statistical data.

In the present work turbulent natural convection at low and medium Rayleigh numbers is directly simulated numerically by the TURBIT-3 computer code (Grötzbach 1979) based on the complete, three-dimensional, non-steady-state equations of the conservation of mass, momentum and enthalpy. The aim of this work is to show that by use of currently available computer systems this three-dimensional scheme may be applied to the Rayleigh–Bénard convection of air with Rayleigh numbers up to 381 225 without using a subgrid-scale model. Generally, agreement with experimental data can be obtained for all flow conditions and for most of the statistical data of the flow fields. The only condition for obtaining reasonable results is the use of nearly randomly distributed initial values and sufficiently fine grids. For the highest Rayleigh number, for instance, this agreement can be obtained from simulations using 32×16^2 mesh points. Increasing the node numbers up to 64×32^2 shows that about $32^2 \times 16$ mesh points are required to get results largely independent of the grids.

2. Basic equations of the method of simulation

2.1. *Basic equations of motion*

The basic equations for laminar and turbulent convection are the equations for the conservation of mass, momentum and energy. For simplicity, the Boussinesq approximation is adopted. This implies the assumption that the physical properties in all terms of these equations can be considered as constant, except for the buoyancy term. If Cartesian co-ordinates are used with x_1 and x_2 horizontal and x_3 directed upwards then the equations for the velocity components u_i ($i = 1, 2, 3$), pressure p and temperature T are

$$\frac{\partial u_i}{\partial x_i} = 0, \tag{1a}$$

$$\frac{\partial u_i}{\partial t} + \frac{\partial u_i u_j}{\partial x_j} = -\frac{\partial p}{\partial x_i} - \frac{Ra}{Pr\,Re_0^2}(T_{\text{ref}} - T)\,\delta_{i3} + \frac{\partial}{\partial x_j}\left(\frac{1}{Re_0}\frac{\partial u_i}{\partial x_j}\right), \tag{1b}$$

$$\frac{\partial T}{\partial t} + \frac{\partial T u_j}{\partial x_j} = \frac{\partial}{\partial x_j}\left(\frac{1}{Pr\,Re_0}\frac{\partial T}{\partial x_j}\right). \tag{1c}$$

The Einstein summation rule is applied to all terms bearing the same subscript twice. Equations (1) are normalized with the plate spacing $\hat{D}$ (variables marked by $\hat{\ }$ are dimensional), the difference in temperatures between the bottom and top walls $\Delta \hat{T}_{\text{w}} = \hat{T}_{\text{w}1} - \hat{T}_{\text{w}2}$, the time scale $\hat{t} = \hat{D}/\hat{u}_0$, and the pressure $\hat{p} = \hat{\rho}\hat{u}_0^2$, where $\hat{\rho}$ is the density. Thus the dimensionless numbers used are the Reynolds number $Re_0 = \hat{u}_0\hat{D}/\hat{\nu}$, the Prandtl number $Pr = \hat{\nu}/\hat{a}$, and the Rayleigh number, $Ra = \hat{g}\hat{\beta}\,\Delta\hat{T}_{\text{w}}\,\hat{D}^3/\hat{\nu}\hat{a}$, where

$\hat{g}$ is the acceleration due to gravity, $\hat{\beta}$ is the volume-expansion coefficient, $\hat{\nu}$ is the kinematic viscosity and $\hat{a}$ is the temperature-conductivity coefficient. The velocity scale $\hat{u}_0 = (\hat{g}\hat{\beta}\Delta\hat{T}_w\hat{D})^{\frac{1}{2}}$ was chosen so as to normalize the buoyancy term to unity. The reference temperature T_{ref} in the buoyancy term is set equal to the volume average in the entire channel $^v\langle T\rangle$, in order to avoid a net contribution to the buoyancy term.

2.2. *Numerical model*

Finite-difference formulas for the numerical solution of the differential equations (1) are derived by the method also used by Schumann (1973, 1975 a). These equations are integrated formally over the mesh volume $V = \Delta x_1 \Delta x_2 \Delta x_3$, which furnishes the volumetric average for any variable y:

$$^v\bar{y} = \frac{1}{\Delta x_1 \Delta x_2 \Delta x_3} \int_{\Delta x_1} \int_{\Delta x_2} \int_{\Delta x_3} y(x_1', x_2', x_3')\, dx_3'\, dx_2'\, dx_1'. \tag{2}$$

By applying Gauss's theorem, the volume average of the partial derivatives is transformed directly into a finite-difference form of the surface average values $^i\bar{y}$, where i denotes the index of the direction normal to the respective mesh cell surface:

$$^v\overline{\frac{\partial y}{\partial x_i}} = \frac{1}{\Delta x_i}[^i\bar{y}(x_i + \tfrac{1}{2}\Delta x_i) - {}^i\bar{y}(x_i - \tfrac{1}{2}\Delta x_i)] = \delta_i{}^i\bar{y}. \tag{3}$$

Application of (2 and 3) to the basic equations (1), together with the splitting of the velocity and temperature fields into spatial averages directly resolved by the grid, $^j\bar{u}_j$, $^v\bar{T}$, and into 'subgrid-scale' parts not resolved spatially, $u_j' = u_j - {}^j\bar{u}_j$, $T' = T - {}^v\bar{T}$, provides a finite-difference formula programmable in an almost-direct manner:

$$\delta_i{}^i\bar{u}_i = 0, \tag{4a}$$

$$\frac{\partial}{\partial t}{}^v\bar{u}_i + \delta_j{}^j\bar{u}_i{}^j\bar{u}_j + \delta_j{}^j\overline{u_i'u_j'} = -\delta_i{}^i\bar{p} - \frac{Ra}{Pr\,Re_0^2}(^v\bar{T}_{\mathrm{ref}} - {}^v\bar{T})\,\delta_{i3} + \delta_j\left(\frac{1}{Re_0}\overline{\frac{{}^j\partial u_i}{\partial x_j}}\right), \tag{4b}$$

$$\frac{\partial}{\partial t}{}^v\bar{T} + \delta_j{}^j\bar{u}_j{}^j\bar{T} + {}^j\overline{u_j'T'} = \delta_j\left(\frac{1}{Pr\,Re_0}\overline{\frac{{}^j\partial T}{\partial x_j}}\right). \tag{4c}$$

The remaining derivatives are approximated according to (3). Adaptation to a staggered grid requires a few additional averages in the convective terms in order to approximate variables between two nodes. A weighted linear average $\bar{y}^j$ is used to account for grids with variable mesh widths Δx_i:

$$\bar{y}^j(x_j + \tfrac{1}{2}\Delta x_j) \simeq \frac{y(x_j + \Delta x_j)\,\Delta x_j(x_j + \Delta x_j) + y(x_j)\,\Delta x_j(x_j)}{\Delta x_j(x_j + \Delta x_j) + \Delta x_j(x_j)}. \tag{5}$$

This results in the following explicit finite-difference scheme, written without space-averaging bars, where the superscript n refers to the time step, $t^n = n\Delta t$:

$$(\tilde{u}_i^{n+1} - u_i^{n-1})/2\Delta t = -\delta_j(\bar{u}_j^i\bar{u}_i^j)^n + \delta_j\left(\frac{1}{Re_0}\delta_j u_i - {}^j\overline{u_i'u_j'}\right)^{n-1} - \frac{Ra}{Pr\,Re_0^2}(^v\bar{T}_{\mathrm{ref}} - {}^v\bar{T})^n\,\delta_{i3},$$
$$\tag{6a}$$

$$(T^{n+1} - T^{n-1})/2\Delta t = -\delta_j(u_j\bar{T}^j)^n + \delta_j\left(\frac{1}{Pr\,Re_0}\delta_j T - {}^j\overline{u_j'T'}\right)^{n-1}. \tag{6b}$$

The pressure p^n is determined from a Poisson equation

$$\delta_i\delta_i p^n = \delta_i\tilde{u}_i^{n+1}/2\Delta t, \tag{7}$$

so that the new time-level velocities

$$u_i^{n+1} = \tilde{u}_i^{n+1} - (2\Delta t)\,\delta_i p^n \tag{8}$$

satisfy the continuity equation (4a). Equation (7) is solved by a fast Fourier transform. Equations (6a, b) correspond to a leapfrog scheme, starting with an Eulerian step and interrupted by an averaging step after every n_L time steps (typically, $n_L = 40$). The permissible size of the time step is determined from a linear stability analysis (Schumann 1975b).

The accuracy of this finite-difference scheme was thoroughly tested by Schumann (1973) on equidistant and non-equidistant grids for non-buoyant flows. Highly non-uniform grids were employed successfully in simulations of annular flows with small ratios of radii (Grötzbach 1977). (The actual computer code is written for both Cartesian and cylindrical co-ordinate systems.)

2.3. *Turbulence assumptions*

The well-known closure problem in connection with the Reynolds equations averaged over time by analogy occurs in (4). The unknown shear stresses $^j\overline{u_i' u_j'}$ and heat fluxes $^j\overline{u_j' T'}$ appearing in (4) contain only the part of the turbulent exchange not resolved by the grid. Thus they tend to zero, if highly resolving grids ($\Delta x_i \rightarrow 0$) are used. This is true in particular of applications to small Rayleigh numbers, since in these cases only very large vortices are formed, which are of the magnitude of the channel width.

In all simulations reported below the subgrid-scale structure terms are neglected, which means that $^j\overline{u_i' u_j'} = {}^j\overline{u_j' T'} = 0$. Thus the entire system of equations does not contain a single adjustable parameter, except for the problem-identifying parameters Ra and Pr, and for the choice of the grid. It must only be ensured that the mesh grid resolves even the smallest relevant turbulence elements. It is shown in the appendix that this assumption is valid for the finest grids used here.

2.4. *Boundary conditions*

In both horizontal directions of the plane channel considered, periodic boundary conditions are used for all velocity components, pressure and temperature. The respective periodicity lengths $X_1 = IM\Delta x_1$ and $X_2 = JM\Delta x_2$ are prescribed in the number of meshes IM and JM, and the mesh widths Δx_1 and Δx_2. For the diffusive terms at the walls the no-slip wall conditions and the wall heat fluxes have been formulated corresponding to the laminar-flow condition proposed by Grötzbach (1977) and Grötzbach & Schumann (1979), which means that linear finite-difference approximations are used. The major drawback in this approximation is that extremely fine meshes must be used in the x_3 direction near the wall to resolve the steep gradients in the temperature field. This is especially true of high Rayleigh numbers. The boundary condition for the pressure $\delta_3 p = 0$ at the walls follows from (8) and the boundary conditions $u_3^{n+1} = \tilde{u}_3^{n+1} = 0$ at the walls.

3. Initial values and case specifications

To start the time integration of the basic equations, initial values are required for the velocity and temperature fields. In order to shorten the computer time required to reach fully developed equilibrium, the statistical properties of the initial values should be very close to the steady-state solutions. There is no general restriction in the

Case	Ra	IM	JM	KM	Δx_1	Δx_2	Δx_{3w}	NT	t_{max}	NM
1	1500	16	16	8	0·175	0·175	0·125	500	25·05	1
2	4000	16	16	8	0·175	0·175	0·125	1060	71·45	1
3	7000	16	16	8	0·175	0·175	0·125	1060	84·95	1
4	87300	16	16	8	0·175	0·175	0·125	1060	85·4	1
5	87300	16	16	8	0·175	0·175	0·0625	1200	84·1	1
6	87300	16	16	16	0·175	0·175	0·02	1880	33·5	1
7	381225	16	16	16	0·175	0·175	0·02	1320	41·01	8
8	381225	32	16	16	0·175	0·175	0·02	920	28·49	8
9	381225	32	16	16	0·088	0·175	0·02	920	26·85	8
10	381225	16	2	16	0·175	0·175	0·02	2000	67·33	26
11	381225	32	2	16	0·175	0·175	0·02	2280	75·0	33
12	381225	32	32	16	0·088	0·088	0·02	3680	100·7	40
13	381225	32	32	32	0·088	0·088	0·01	5040	42·7	64
14	381225	64	32	32	0·044	0·088	0·01	3880	32·7	31

TABLE 1. Case specifications and time intervals simulated. $\Delta x_{3w} = \Delta x_{3K=1}$ = vertical grid width near the wall. The complete vertical profile of Δx_3 is given in table 4.

statistical properties of the initial values, except for the flow structures in these fields. To avoid the pre-determination of special roll vortex patterns by the choice of initial values, all velocity fields are set to zero at the time $t = 0$. The temperature fields are chosen in such a way that the vertical profiles of the statistical averages in the flow core agree with the experimental results. The approximately linear temperature curves found in the centre between the plates are linearly extrapolated to the walls. Random temperature variations have been superimposed upon these temperature fields, with maximum amplitudes of $T' = \pm 0·05$. This is necessary, as the onset of convection is caused by a disturbance.

Further input data for the computer simulation of Bénard convection are the molecular Prandtl number of air ($Pr = 0·71$), the Rayleigh number and the grid parameters (table 1). The Rayleigh numbers in cases 1–3 were selected to represent at least one simulation for each flow condition according to the flow regime diagram of Krishnamurti (1973). The other cases were chosen for direct comparison with the experimental results of Thomas & Townsend (1957). Different grids were chosen to analyse influences of different mesh spacings on the simulated convection. Results by Lipps (1976) show such influences, especially for low Rayleigh numbers. Therefore special emphasis was put on finding the maximum-allowable grid width and the influence of the periodicity lengths for the high-Rayleigh-number simulations. In particular, cases 12–14 have been taken from Grötzbach (1980) to confirm the high-Rayleigh-number simulations of this work.

4. Numerical results

Starting from initial values defined above, (6)–(8) were integrated in the time domain until largely steady-state conditions, in a statistical sense, had been established for a period suitable for evaluation. The respective number of time steps NT and problem duration time t_{max} are indicated in table 1. The CPU times consumed on an IBM 370/168 are about $460 \mu s$ per mesh cell and time step, which results in a total CPU time of 58 min, for example, for cases 8 and 9.
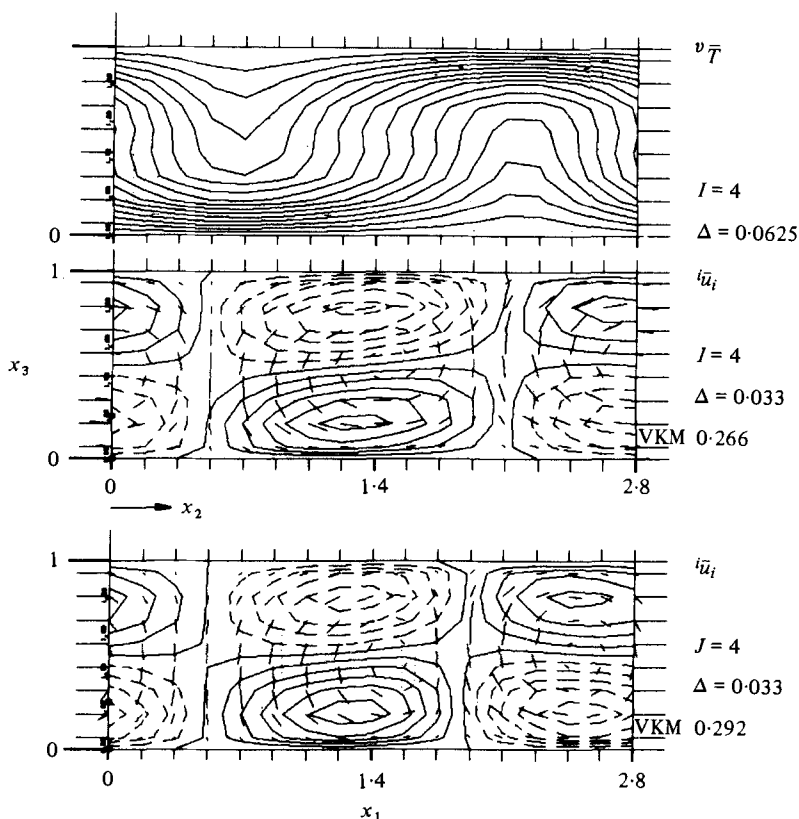
FIGURE 1. Vertical sections of the temperature and velocity fields at $t = 68.4$ for $Ra = 4000$. The sectional planes (from top to bottom) are the (x_2, x_3)-plane, (x_2, x_3)-plane and the (x_1, x_3)-plane. VKM is the maximum vector length, Δ is the contour-line increment. The mesh indices I, J denote the positions of the cross-sections $x_1 = (I-1)\,\Delta x_1$ and $x_2 = (J-1)\,\Delta x_2$.

4.1. *Phenomenological evaluation of the results of simulation*

The numerical results are compared qualitatively on the basis of contour-line and vector representations of the instantaneous velocity and temperature fields (figure 1–7). For the velocity field the isolines show the values of the component normal to the drawing plane. The isoline increment Δ is constant. Non-negative values are represented by solid lines, negative values by dashed lines. The additional dashes indicate the magnitude and directions of the velocities in the plotting plane. The origin of the dashes is located at the respective nodal point of a mesh.

For the subcritical case with $Ra = 1500$ the convection caused by the initial conditions tends to zero. The conduction-controlled temperature field remains unchanged by the decreasing convection. The resultant stratification behaves in a stable mode. This is in accordance with experiments performed for different Prandtl numbers for $Ra < 1708$ (Brown 1973; Krishnamurti 1973; Silveston 1958).

Vertical sections of the velocity and temperature fields for $Ra = 4000$ are represented in figure 1 for one of the last time steps of simulation. The temperature field undergoes major distortions in the directions of convection. All fields are well arranged, which is indicative of laminar convection. The related horizontal section in figure 2 indicates the presence of vortex pairs whose horizontal axes extend diagonally through the grid.
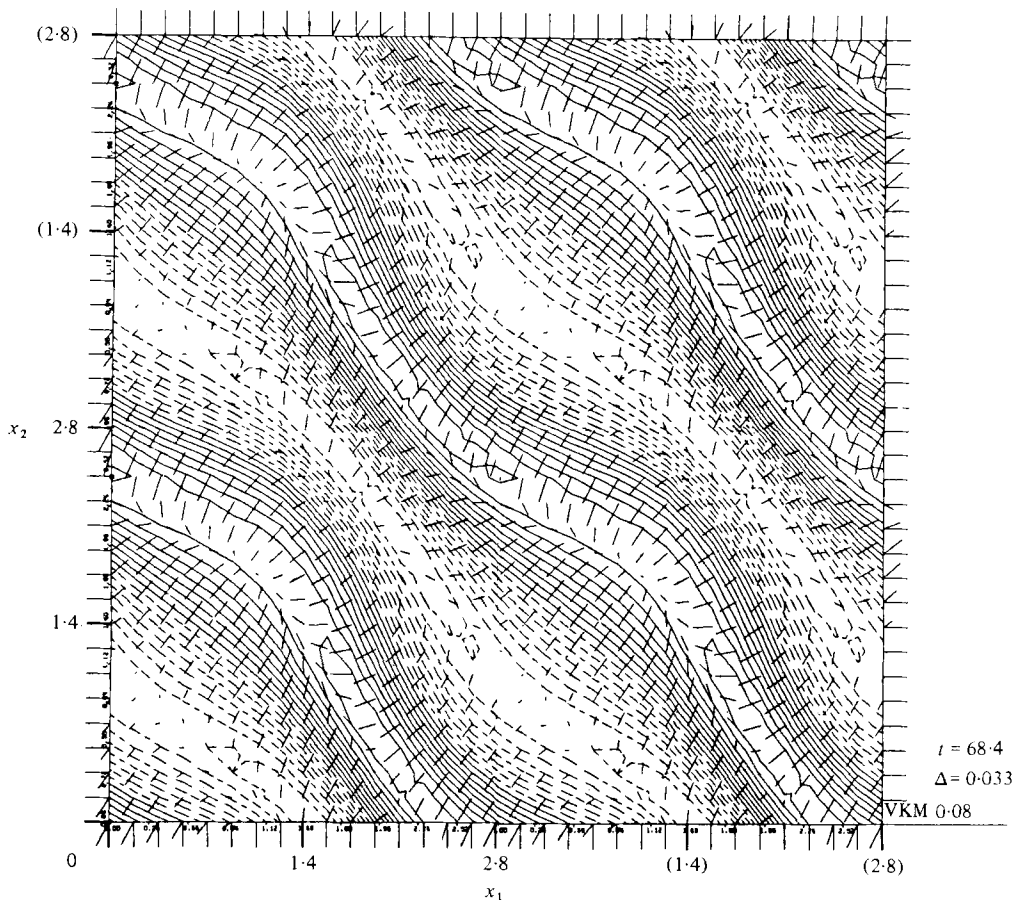
FIGURE 2. Horizontal section of the velocity field at $t = 68\cdot4$ and $x_3(K = 4) = 0\cdot438$ for $Ra = 4000$. $\Delta = 0\cdot033$ and VKM $= 0\cdot08$. The figure consists of four identical plots. The mesh index K denotes the position of this cross-section according to table 4 and

$$x_3(K) = \sum_{n=1}^{K-1} \Delta x_3(n) + \tfrac{1}{2}\Delta x_3(K).$$

For better identification of this stationary flow regime this figure was composed out of four identical plots. As a result, space-periodic enlargements and contractions of the regions of upward and downward flows can be identified. This can be interpreted as a so-called 'skewed-varicose' flow regime and is known to occur for larger Prandtl numbers, as was shown by Busse & Clever (1979).

For $Ra = 7000$ the different sections of the velocity fields show that non-steady-state three-dimensional vortex structures are formed (figures 3 and 4). This is a vortex pair whose sense of rotation does not depend on time. The periodicity of the field as a function of time can be deduced from the u_3 isolines in figure 4. It is obvious from the horizontal sections that the axes of vortices pointing in the x_1 direction are deflected in the x_2 direction with a period $\tau = 16\cdot9$. The three-dimensional periodic flow found here for $Ra = 7000$ agrees with the experimental results of Willis & Deardorff (1965) and Krishnamurti (1973).

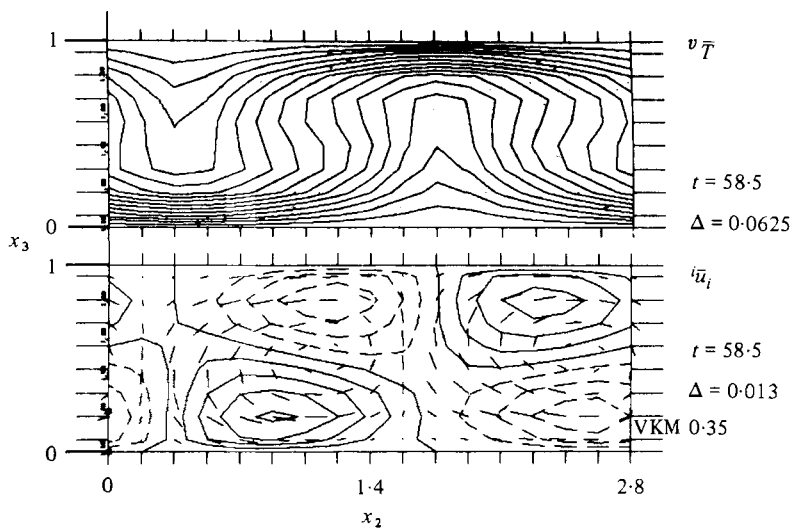A vertical section of the temperature field has been included in figure 3. The

G. Grötzbach

FIGURE 3. Vertical sections of the temperature and velocity fields for
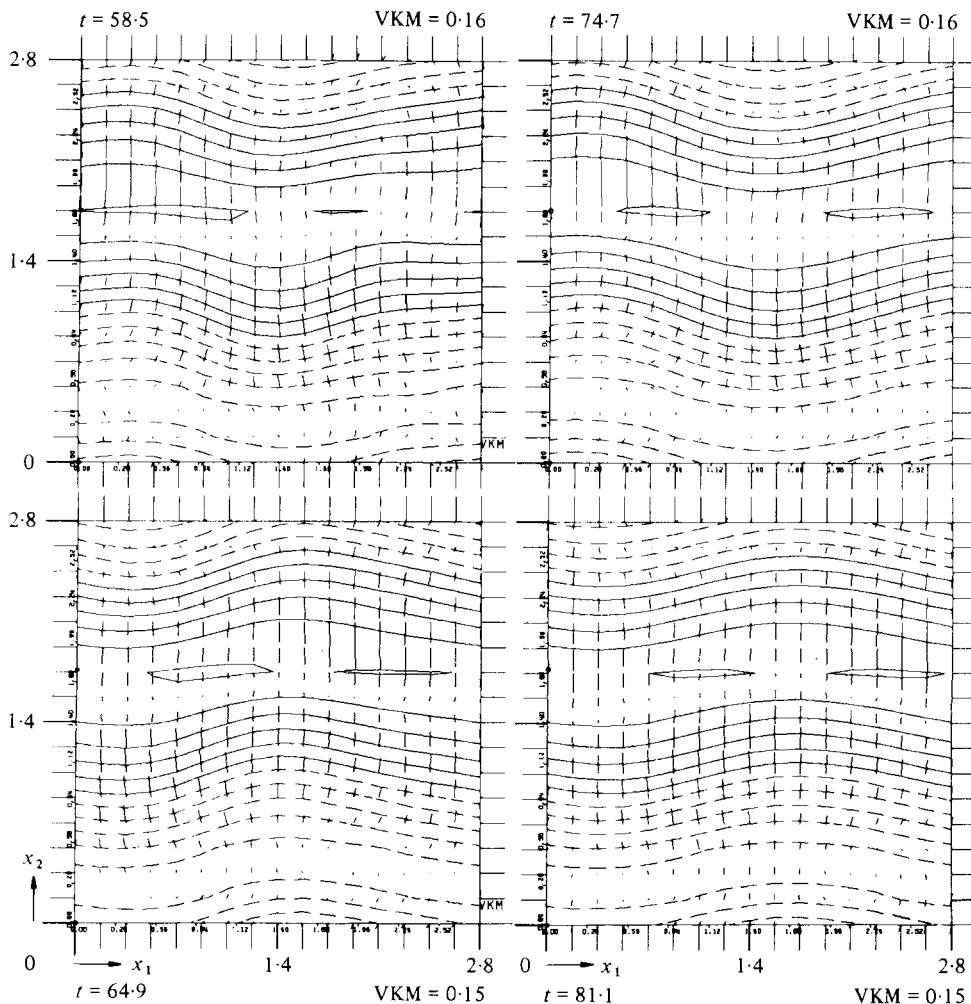$I = 4$ and $Ra = 7000$; (x_2, x_3)-plane.

FIGURE 4. Horizontal sections of the velocity fields at different times
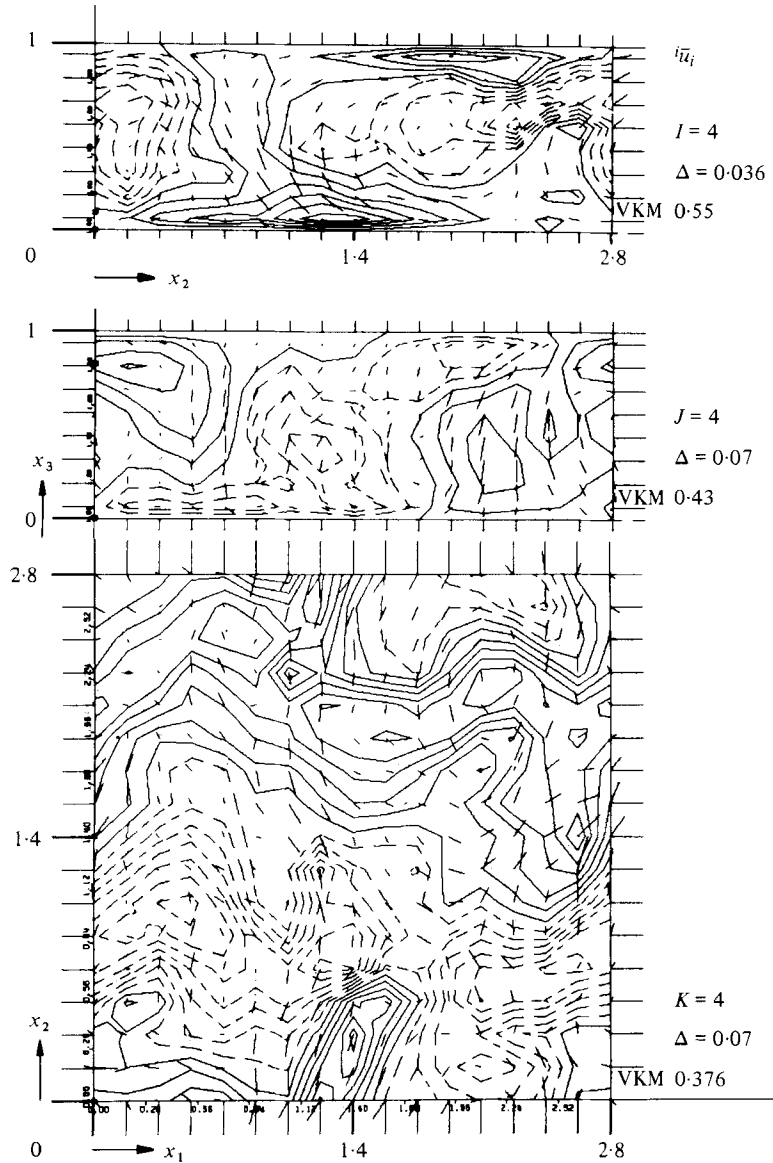for $x_3(K = 4) = 0.438$ and $Ra = 7000$; $\Delta = 0.05$.

FIGURE 5. Vertical and horizontal sections of the velocity
field for $t = 67.3$ and $Ra = 87300$; case 4.

isotherms are shifted in the directions of the flow. Higher heat-transfer values occur locally in the vicinity of the stagnation points at the walls. Moreover, near these zones the isotherms expand more strongly in the horizontal direction than for $Ra = 4000$. Consequently, the vertical temperature profile in the middle between the upward and downward flows shows a local change of sign in its vertical gradients.

The velocity field for $Ra = 87300$ shown in figure 5 has no regular structures. The randomized nature of the fields indicates a fully turbulent flow. This conclusion can also be drawn from the time sequence of vertical sections through the temperature field represented in figure 6. The upward movement of hot fluid and the downward
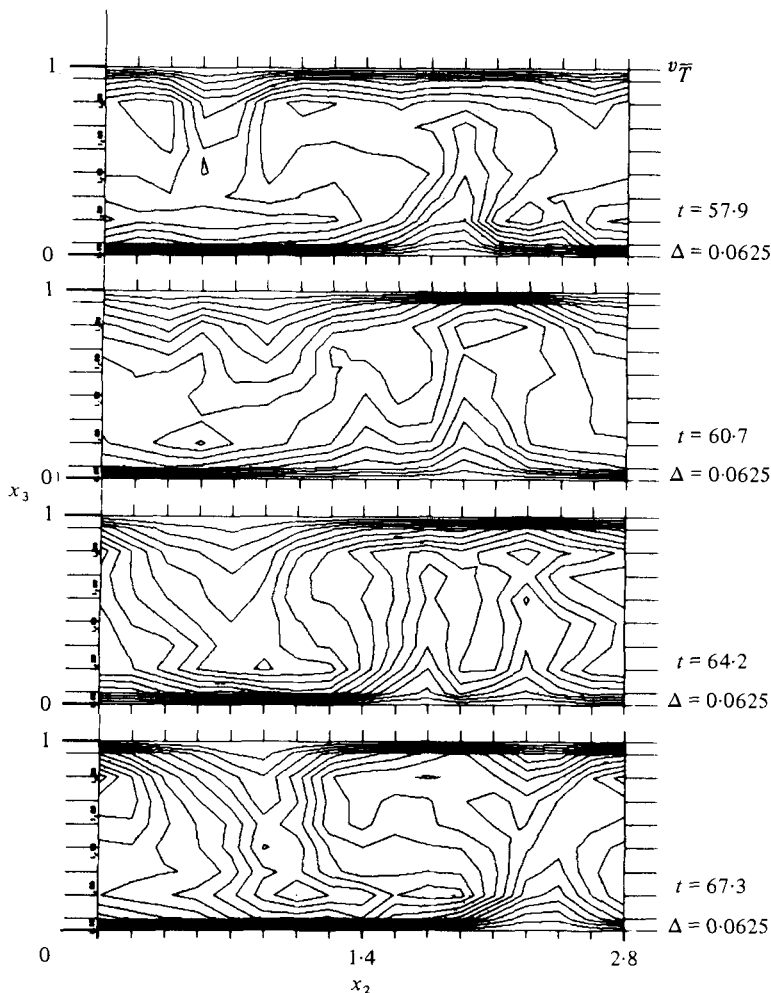
FIGURE 6. Vertical sections of the temperature field at different
times for $I = 4$ and $Ra = 87300$, case 4; (x_2, x_3)-plane.

movement of cold fluid is irregular and aperiodic. This is in accordance with experi-
mental results of Krishnamurti (1973) and Willis & Deardorff (1965), which show
turbulent convection at $Ra > 10\,000$ for $Pr = 0.71$.

The vector and isoline representations in figure 7 for $Ra = 381\,225$ largely corre-
spond to those in figures 5 and 6. However, the degree of irregularity has increased
slightly. Besides, the spatial extension of the structures encountered has decreased.
The spatial extension of the smallest structures recorded is comparable to the grid
width.

4.2. Statistical evaluation of the results of simulation

For quantitative comparison of the numerical results with the statistical data deter-
mined experimentally, the non-steady-state numerical results must be evaluated and
averaged appropriately. For this purpose, average values are formed over horizontal
planes. In some cases, these values in addition have been averaged over NM time steps
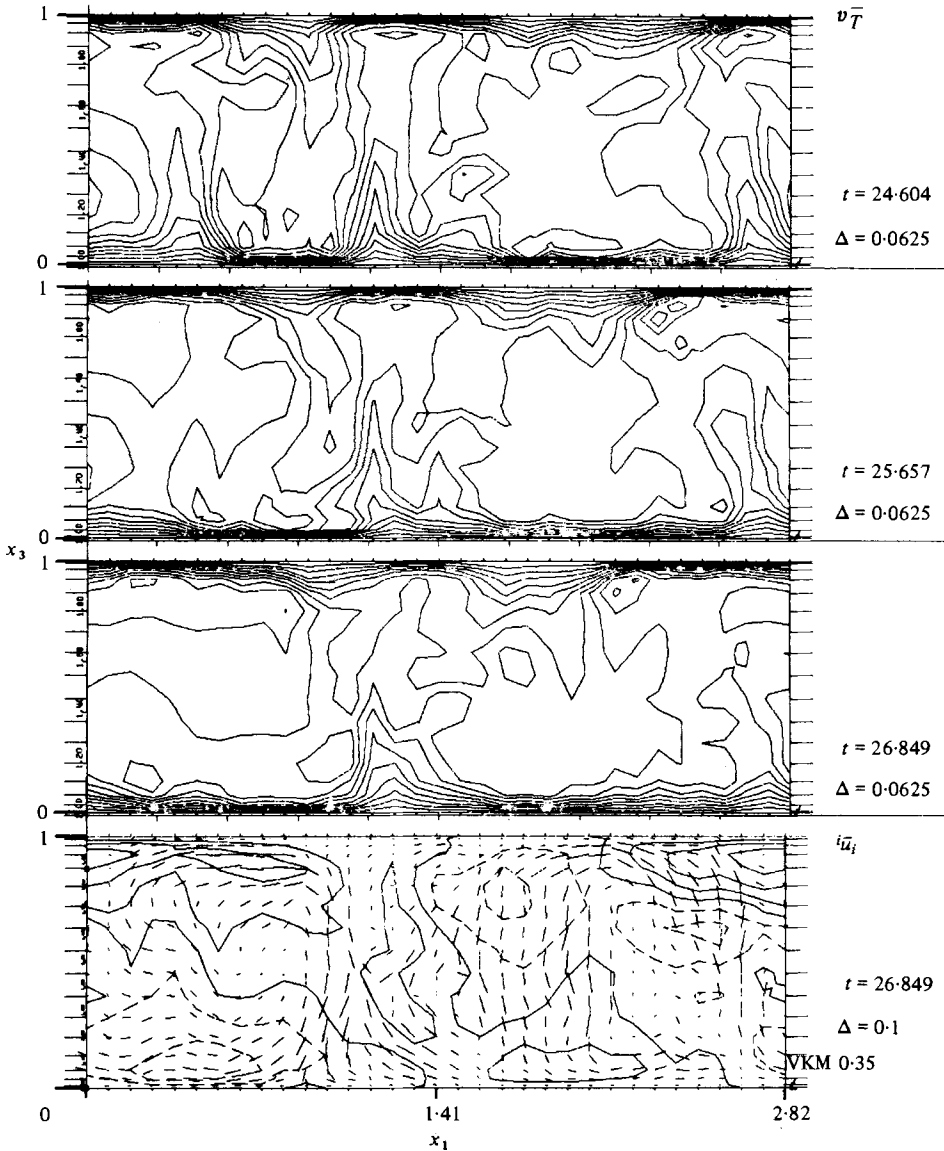
FIGURE 7. Vertical sections of the temperature and velocity fields at different times for $J = 4$ and $Ra = 381\,225$, case 9; (x_1, x_3)-plane.

(table 1) to furnish long-term averages. In such time averaging the results for every 40th time step have been used. The notation for such averages is $\langle y \rangle$.

The Nusselt number has been evaluated on the basis of the dimensionless relation $Nu = (\dot{q}_{conv} + \dot{q}_{cond})/\dot{q}_{cond} = \langle \dot{q}_w \rangle Re_0 \, Pr/\langle \Delta T_w \rangle$ for the convective and conductive heat fluxes. The results have been compiled in table 2. To compare these results with experimental data the coefficient c_q of the heat transfer law $Nu = c_q Ra^{\frac{1}{3}}$ has been calculated and plotted (figure 8), as was proposed by Denton & Wood (1979). The numerical results concerning cases with high spatial resolution are in agreement with the interpolation formula given by Busse & Whitehead (1974): $Nu = 0.19 \times Ra^{0.282}$.

Case	Ra	Nu	Modification (see table 1)	$(\langle{}^1\bar{u}_1'^2\rangle_{max})^{\frac{1}{2}}$	$(\langle{}^2\bar{u}_2'^2\rangle_{max})^{\frac{1}{2}}$	$(\langle{}^3\bar{u}_3'^2\rangle_{max})^{\frac{1}{2}}$	$(\langle{}^v\bar{T}'^2\rangle_{max})^{\frac{1}{2}}$	$\left\langle \dfrac{\langle{}^3\bar{u}_3'{}^v\bar{T}'\rangle}{(\langle{}^3\bar{u}_3'^2\rangle)^{\frac{1}{2}}(\langle{}^v\bar{T}'^2\rangle)^{\frac{1}{2}}} \right\rangle$
1	1 500	1·0	—	→0	→0	→0	→0	—
2	4 000	2·0	—	0·13	0·142	0·202	0·184	—
3	7 000	2·3	—	0·31	0·25	0·189	0·199	—
4	87 300	5·41	—	0·15	0·206	0·215	0·143	—
5	87 300	4·51	Δx_{3w}	0·151	0·215	0·202	0·152	—
6	87 300	4·94	Δx_{3w}, KM	0·173	0·165	0·234	0·161	—
7	381 225	7·75	—	0·163	0·180	0·207	0·166	—
8	381 225	7·74	IM	0·175	0·143	0·213	0·163	0·758
9	381 225	7·44	Δx_1	0·151	0·163	0·207	0·157	0·67
10	381 225	8·6	2-dimensional	0·250	0·086	0·253	0·167	0·659
11	381 225	8·5	2-dimensional, IM	0·244	0·07	0·261	0·164	0·724

TABLE 2. Numerical results for the Nusselt number, the maximum r.m.s. values for the fluctuations of the three velocity components and of the temperature, and for the channel-averaged value of the heat flux cross-correlation coefficient
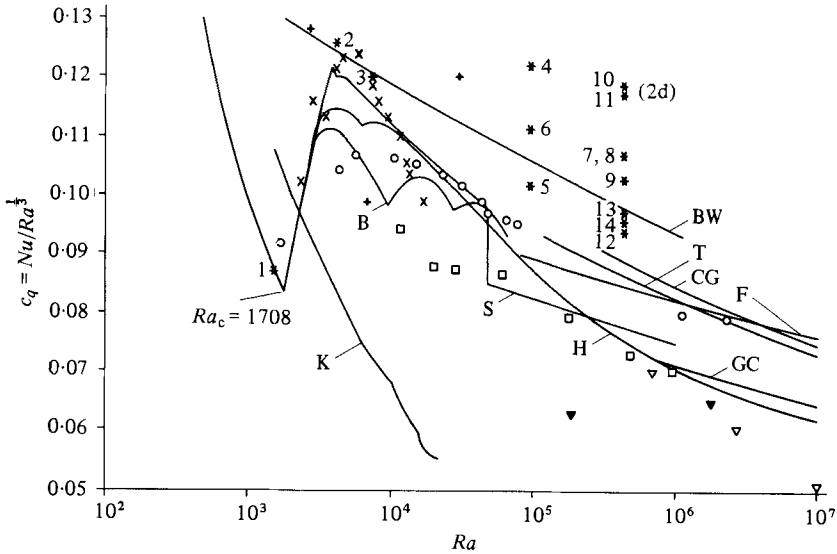
FIGURE 8. Comparison of the normalized Nusselt numbers derived from the numerical simulations with experimental results. 2d denotes the results for the approximately two-dimensional simulations, cases 10 and 11, which are discussed in the appendix.▼, Deardorff & Willis (1965), air; ▽, Deardorff & Willis (1967), air; +, Gille (1967), air; ×, Krishnamurti (1970), water; □, Malkus (1954), water; ○, Threlfall (1975), helium; B, Brown (1973), air; BW, Busse & Whitehead (1974), $Pr = 20$–200; CG, Chu & Goldstein (1973), water; F, Fitzjarrald (1976), air; GC, Goldstein & Chu (1969), air; H, Hollands, Raithby & Konicek (1975), air; K, Krishnamurti (1973), air; S, Silveston (1958), water; T, Threlfall (1975), helium; *, TURBIT-3, this work, air, case no.

The other experimental data deviate from each other and from the numerical results.

In non-turbulent flows with Rayleigh numbers $Ra < 10000$ vortex systems are formed that consist of vortex pairs with an overall diameter λ. Owing to the fact that $\lambda > D$ and the periodic boundary conditions, only discrete values of λ can be obtained from the numerical results. Depending on whether the axes of vortices are parallel to the x_2 axis or to the x_1 axis or run diagonally through the grid, the following maximum values can occur: $\lambda = X_1$, X_2, $[(\frac{1}{2}X_1)^2 + (\frac{1}{2}X_2)^2]^{\frac{1}{2}}$. The possible values of λ and the observed ones have been included in table 3. The values indicated for the laminar cases have been evaluated from figure 2 and 4. Upper bounds of the values of the turbulent cases were obtained by evaluation of the two-point correlation R_{33} in the x_1-direction. R_{ii} is defined as (no summation over i)

$$R_{(i)(i)}(z) = \frac{\langle {}^i\bar{u}'_{(i)}(x_1, x_2, x_3)\, {}^i\bar{u}'_{(i)}(x_1 + z, x_2, x_3)\rangle}{\langle {}^i\bar{u}'^2_{(i)}(x_1, x_2, x_3)\rangle}.$$

Figure 9 represents these two-point correlations for cases 6 and 8. At half the periodicity length the correlations for case 6 with $Ra = 87\,300$ still differ greatly from zero. This means that either the selected periodicity length X_1 was assigned too low a value for statistical decoupling within different zones of the flow volume recorded, or the axes of vortices lie mainly in the x_1 direction. This plot at the most permits the conclusion to be drawn that $\lambda \simeq X_1$. The respective curves for case 8 with $Ra = 381\,225$ and the double periodicity length $X_1 = 5\cdot6$ tend towards zero for the distance $z \simeq \frac{1}{2}X_1$.

Case	$\lambda_{\text{max poss}}$			$\lambda_{\text{max obs}}$	Case
1–7, 9	2·8	2·8	1·98	1·66–2·22	2
				2·8	3
8	5·6	2·8	3·13	1·75–1·86	8
10	2·8	~ 0	~ 0	$\sim 1·4$	10
11	5·6	~ 0	~ 0	$\sim 1·4$	11

TABLE 3. Maximum possible and observed vortex dimensions
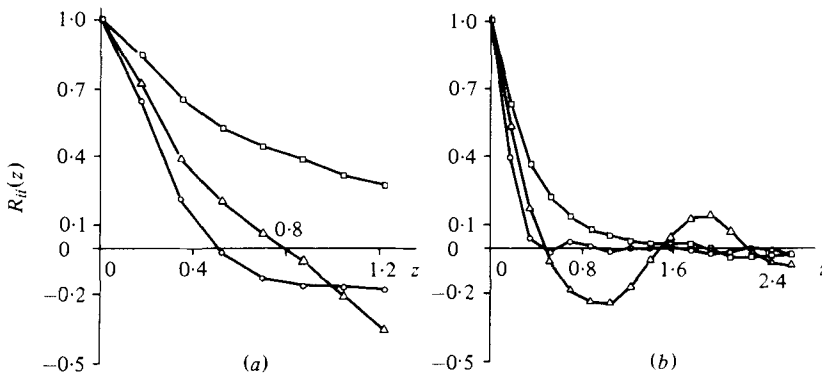for the grids, according to table 1

FIGURE 9. Two-point correlations R_{ii} of the velocity fluctuations $^i\bar{u}'_i = {}^i\bar{u}_i - \langle {}^i\bar{u}_i \rangle$ in the x_1 direction for (a) $Ra = 87300$, case 6; and (b) $Ra = 381225$, case 8. $\square$, R_{11}; $\bigcirc$, R_{22}; $\triangle$, R_{33}.

A range for the upper bound for λ can be estimated to be 1·75–1·86. This follows from the distance between the extreme values of the same sign or from the assigned intersections of the z-axis by R_{33}.

In figure 10 the numerical results of cases 2 and 3 have been compared with the experimental results of Willis, Deardorff & Somerville (1972) and Brown (1973). The value of $Ra = 4000$ is lower than the value observed most frequently, although the grid would allow a higher value. The result for $Ra = 7000$ agrees with the maximum possible value for this grid.

Following the definition of the root-mean-square value

$$y_{\text{rms}} = \langle y'^2 \rangle^{\frac{1}{2}} = \langle (y - \langle y \rangle)^2 \rangle^{\frac{1}{2}}$$

the peaks of the vertical r.m.s. value profiles of the three velocity components derived from the space- and time- dependent results have been represented in table 2 and figure 11. For $Ra = 1500$ all r.m.s. values are close to zero. Within the transition zone to turbulent flow ($Ra < 10^4$) the r.m.s. values increase strongly. The u_1 and u_2 components should be equal in size. The dissimilar values show that the values indicated suffer from a 20 % uncertainty because of the low mesh number and on account of the evaluation of only one time step ($NM = 1$, table 1). In the fully turbulent zone the r.m.s. values are independent of the Rayleigh number. For comparison the experimental results by Deardorff & Willis (1967) have been included in figure 11.

The influence of the Rayleigh number on the averaged vertical temperature profile and on the r.m.s. temperature value is indicated for cases with sufficient spatial
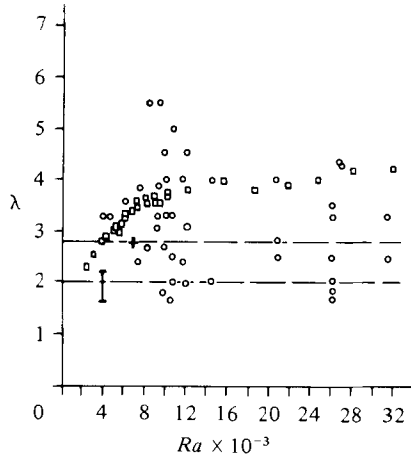
FIGURE 10. Vortex dimension λ as a function of the Rayleigh number. The dashed lines mark the two possible maximum values in the corresponding grids according to table 3. $\square$, Willis *et al.* (1972); $\bigcirc$, Brown (1973), $+$, I, TURBIT-3.
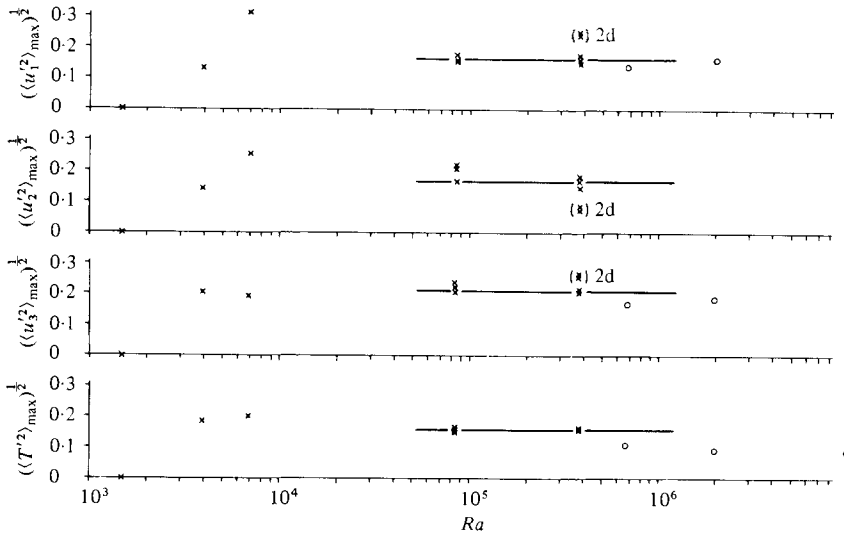

FIGURE 11. Maximum r.m.s. values of velocity and temperature fluctuations. 2d denotes the results for the approximately two-dimensional simulations, cases 10 and 11, which are discussed in the appendix. $Pr = 0.71$; $\bigcirc$, Deardorff & Willis (1967); $\times$, TURBIT-3.

resolution in figure 12. The temperature profiles are more or less point-symmetrical with respect to the channel centre. For $Ra = 1500$ the profile is linear. With increasing Rayleigh number the gradient at the wall becomes steeper owing to the increasing importance of convection, and the temperature profile inside the channel becomes nearly constant. For $Ra = 7000$ and $87\,300$ temperature inversions are observed.

The r.m.s. temperature values are also shown in figure 12. With decreasing Rayleigh number the peak moves away from the wall until it lies in the centre of the channel for $Ra = 4000$. For $Ra = 1500$ the r.m.s. values over the whole zone are zero. While the vertical temperature profiles are sufficiently well resolved by the predominately non-
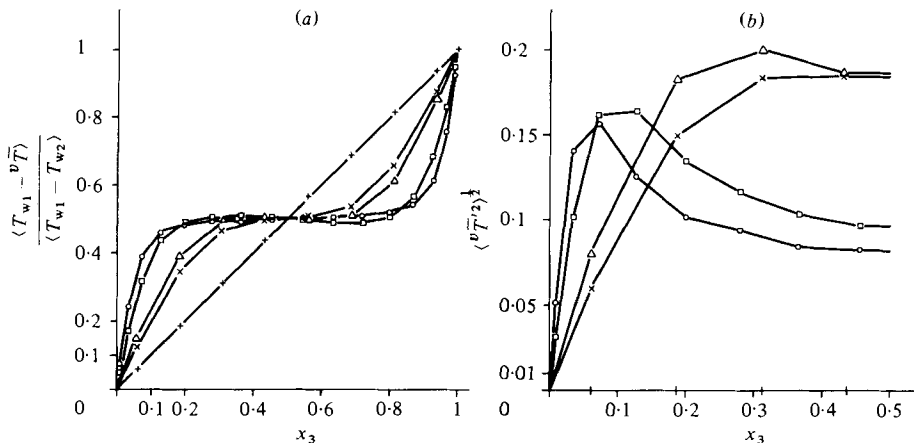
FIGURE 12. Averaged vertical temperature (a) and r.m.s. temperature value (b) profiles for different Rayleigh numbers. +, $Ra = 1500$, case 1; ×, 4000, 2; △, 7000, 3; □, 87 300, 6; ○, 381 225, 9.

equidistant vertical mesh distributions selected, finer resolution would be desirable for a more accurate determination of the location of the r.m.s. temperature peaks (see also the appendix).

5. Discussion of numerical results

The computer model used includes no adjustable parameters such as model constants or empirical wall functions. The influence of the grids selected is discussed in the appendix and in Grötzbach (1980). It becomes evident there that the spatial resolution of most of the grids used in this work is sufficient for an accuracy comparable to that usually obtained in laboratory experiments, despite the fact that the grids used for cases 7–9 do not really resolve the smallest scales of turbulence. These are only resolved by the grids of cases 12–14, which give more accurate results. In this section significant results will be discussed and some discrepancies between calculated and experimental data, which seem to exist despite sufficient spatial resolution.

5.1. Discussion of phenomenological results

Qualitative evaluation of the numerical results shows that the flow caused by the randomly disturbed initial fields disappears at a Rayleigh number below the critical values as expected; the layer is stable. At the next higher Rayleigh number, $Ra = 4000$, a steady-state flow regime should develop; for example according to the flow regime map of Krishnamurti (1973). That map, however, provides no information about the dimensionality of this flow. Clever & Busse (1978) predicted theoretically a three-dimensional flow regime, which they called 'skewed-varicose' instability. The existence of this flow regime has been confirmed for higher Prandtl numbers in the experiments of Busse & Clever (1979). Its wavelength has also been detected for $Pr = 0.71$ by Clever & Busse (1978) in the experiments of Willis et al. (1972). The numerical results given in figure 2 show the features discussed above, thus confirming directly the predictions of Clever & Busse (1978) for the Prandtl number under consideration.

If the Rayleigh number is increased to $Ra = 7000$, the three-dimensional flow field

becomes periodic in time. The horizontal axes of the vortices are periodically distorted into serpentines (see figure 4). As suggested by Lipps (1976), the period of oscillation seems to depend strongly on the horizontal periodicity lengths. The periodicity lengths prescribed do not allow the wavelengths observed in experiments to be recorded (figure 10). Nevertheless, the period found here exactly fits the interpolation curve given by Krishnamurti (1973). This difference in results between Lipps' simulation and the present work is due mainly to the initial conditions chosen. In this work the vortex structures calculated are not given in the initial conditions, but are found as a nearly independent result of the numerically simulated physics. Thus from among the infinite number of possible wavelengths the optimal one can be developed freely.

For the two highest Rayleigh numbers, the flow regime map of Krishnamurti (1973) leads one to expect a fully turbulent convection. Indeed, the flow fields given in figures 5–7 are aperiodic and without recognizable regular structures. For the highest Rayleigh number (figures 7 and 16) the smallest scales are comparable to or a little bit smaller than the grid width of case 9. Therefore the finer grids of cases 12–14 should be used, or subgrid-scale structure models will be needed for this and higher Rayleigh numbers.

5.2. *Discussion of statistical results*

5.2.1. *Influence of the wavelength on the convective heat flux.* Experimental results for the characteristic vortex diameter of Willis *et al.* (1972) and Brown (1973) show a continuous increase, with increasing Rayleigh number, in the laminar-to-turbulent transition zone (figure 10). A more stepwise increase at high Rayleigh numbers was found by Fitzjarrald (1976) for a channel with a large aspect ratio. The same author shows the dominant wavelength to decrease with increasing Rayleigh number for a small aspect ratio.

The grids chosen here cannot reflect the maximum wavelengths observed, except for the grid of case 2 (figure 10, table 3). No agreement can therefore be obtained with experimental results, except for case 2. Nevertheless, the wavelengths found in the transition zone are in accordance with the many possible values predicted by stability theory. Consistent with the flow regime found for $Ra = 4000$, the wavelength (table 3) is near the 'skewed-varicose' instability line in the stability map of Busse & Clever (1979) and, for $Ra = 7000$, near the line of the oscillatory instability. In the fully turbulent region the wavelengths decrease with increasing Rayleigh numbers. They are smaller than in the transition zone because small periodicity lengths have been prescribed. The influence of the periodicity lengths on the dominant wavelength is therefore similar to that of the side walls in low-aspect-ratio experiments.

The experimental results and empirical correlations for the normalized Nusselt number (figure 8) deviate from each other; in part there are considerable deviations. For this Prandtl number and others it is still being discussed whether the slope for $Nu = f(Ra)$ undergoes many changes (Krishnamurti 1973; Willis *et al.* 1972; Brown 1973) or not (Koschmieder & Pallas 1974; Fitzjarrald 1976). It is supposed (see e.g. Threlfall 1975; Denton & Wood 1979) that this might be influenced by the differences in the finite spatial extension of the channels used, because very extensive vortex structures have been observed by Deardorff & Willis (1967) in equipment of large horizontal extension. From the work of Lipps & Somerville (1971) and Fitzjarrald

(1976), for example, it is known that such large-scale horizontal flow patterns impede the heat flux. At smaller aspect ratios the dominant wavelength decreases and, consequently, the heat flux is enhanced.

The numerical results for the Nusselt number in figure 8 are at the upper boundary of the scattering range of the experimental data. The results follow the empirical relation by Busse & Whitehead (1974). Although this relation was derived from experiments with Prandtl numbers between 20 and 200, it is nevertheless used for comparison, since Silveston (1958) has shown that no influence of the Prandtl number can be observed in laminar convection, and that the influence is extremely low ($Nu \sim Pr^{0.05}$) in turbulent convection. According to §A.2 in the appendix, the numerical results of case 9 should be lower by about 6 % owing to the limited resolution capabilities of the grid used. Yet all results are about 10 % higher than the experimental data for large aspect ratios, in accordance with the shorter wavelengths developed. In the appendix no considerable influence of the periodicity lengths has been found, except for the nearly two-dimensional simulations which lead to a further decrease of wavelength and, consistently, to an increase in the Nusselt number. Therefore one may assume for three-dimensional convection that the curve for high Prandtl numbers is an upper limit for the Nusselt number at the Prandtl number of air and at small aspect ratios. The empirical correlations for the Nusselt number should include the aspect ratios or periodicity lengths as additional parameters.

5.2.2. *Development of temperature-gradient reversals.* Some of the mean temperature distributions determined experimentally, for example by Gille (1967) and Chu & Goldstein (1973), show gradient reversals in the central region of the channel for Rayleigh numbers up to 5×10^5. This has been attributed to the coalescence of larger numbers of warm 'blobs' near the cold wall and of cold 'blobs' near the warm wall. The temperature profiles determined numerically for $Ra = 7000$ and 87 300 also show gradient reversals (figure 12). For $Ra = 381\,225$ no inversions seem to exist in the temperature profiles. Nevertheless, the eddy conductivity profile calculated for case 14 indicates that slight temperature inversions do exist at this Rayleigh number (Grötzbach 1980).

The corresponding contour-line plots (figures 3, 5, 6 and 16) allow the identification of transient structures, which may be called 'blobs'. There are narrow regions in the central parts of the channel (see e.g. figure 16) with high velocities directed to the walls, where the flow paths end in larger regions of low velocities. This is the mechanism by which hot fluid is transported quickly to the cold wall, where it remains for some time, losing its energy and coming into an equilibrium with the surrounding fluid. The same holds true for cold fluid transported downwards. The possibility of studying such local transient mechanisms easily is an important advantage of the direct numerical simulation technique.

5.2.3. *Consistency of computed turbulence data.* From a data collection by Deardorff & Willis (1967) it can be deduced that the sum of the three r.m.s. values of the time- and space-dependent velocity fluctuations for high Ra is independent of Ra in the present normalization scheme. A similar result was found by Dubois & Bergé (1978) for the transition range at a higher Prandtl number. The numerical results, especially for u_3 and T (figure 11), are also nearly independent of Ra. Major differences appear, however, for the numerical and experimental r.m.s. temperature values. The experimental data are lower and tend to decrease slightly. These problems seem to be associated with the
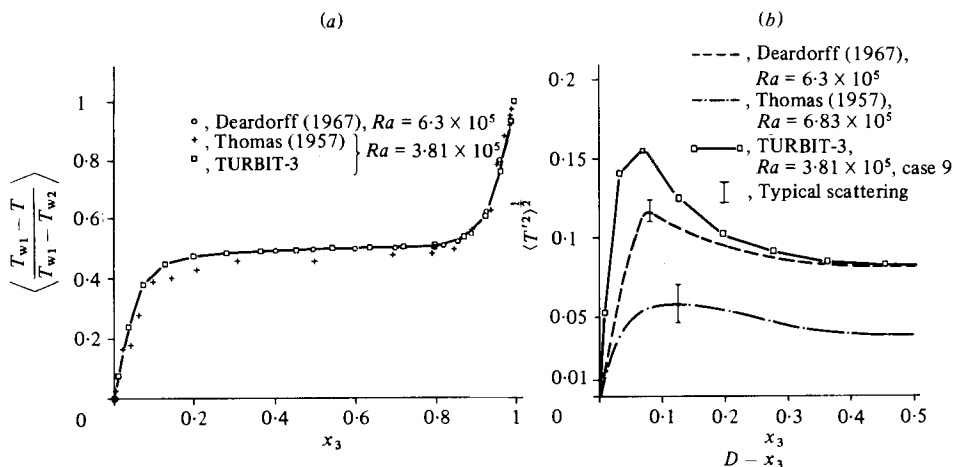
FIGURE 13. Comparison with experimental results of the averaged vertical temperature (*a*) and r.m.s. temperature value (*b*) profiles for $Ra = 381\,225$, case 9.

experimental data, because Fitzjarrald (1976) also obtained results that scattered broadly.

Only those experimental data for which the Boussinesq approximation holds can be used to compare vertical profiles. The temperature profiles of Thomas & Townsend (1957) do not seem to satisfy this condition because of the lack of symmetry with respect to the centre of the channel (figure 13). The data of Deardorff & Willis (1967) obviously satisfy this condition. The numerical results agree with the experimental data elaborated by those authors. The vertical profiles of the r.m.s. temperature values (figure 13) determined by Thomas & Townsend (1957) are 50 % lower than the other data, and the peak is located at a greater distance from the wall. The numerical results agree largely with the experiment by Deardorff & Willis (1967). However, the calculated maximum value is higher by about 30 %. In the appendix it is shown that this deviation is not due to the selection of inadequate grids. Application of finer grids reduces this difference by less than 4 % (table 5). Figure 14 shows the profiles of the r.m.s. values of velocity fluctuations. The differences in the numerical results for u_1 and u_2 are less than 10 %. The values measured by Deardorff & Willis (1967) are almost exactly between the two curves. The r.m.s. values of u_3 rise more slowly, beginning at the wall, than the data measured by Deardorff, and they reach a higher maximum value in the centre of the channel. However, Deardorff's data for the vertical component do not behave uniformly with respect to either the maximum value (figure 11) or the gradient near the wall for different Rayleigh numbers (see Deardorff & Willis 1967).

Indeed, the numerical results can be confirmed by the profile of the vertical heat-flux cross-correlation coefficient, which, by definition, contains r.m.s. values (figure 14). Deardorff's data show a strange suppression near the wall, exactly in the region of the peak of the r.m.s. temperature profile, which is contained neither in the experimental data of Adrian (1975) nor in the numerical result.

5.2.4. *Efficiency of the method used.* Comparison of the computer times of typically one hour with those of Daly's (1974) two-dimensional statistical turbulence model yields the interesting finding that, for the same Rayleigh number, the three-dimensional
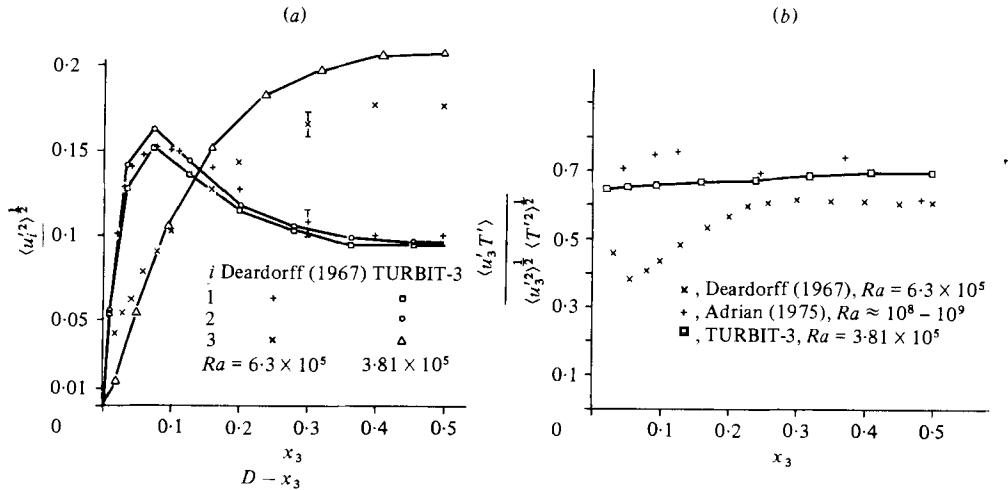
FIGURE 14. Comparison with experimental results of the vertical profiles of the r.m.s. velocity values (a) and of the vertical heat-flux cross-correlation coefficient (b) for $Ra = 381\,225$, case 9.

simulation up to case 9 is faster by roughly one order of magnitude. The main reason for the expenditure involved in Daly's refined statistical turbulence model is its use of seven additional transport equations to model the unknown turbulent shear stresses and heat fluxes. The direct-simulation method does not call for model assumptions, and is therefore suited to advance calculations of cases not previously investigated. Thus these advantages of the direct method are further supplemented by major cost savings.

6. Concluding recommendations

For future investigations of Bénard convection by the method of direct numerical simulation the following recommendations or requirements are derived from the results discussed here: The method of deriving finite-difference formulas for the basic equations using Gauss' theorem is a successful tool for all cases in which highly non-isotropic grids are used. It should be used for such simulations, in connection with a staggered grid, because no major approximations are necessary. To avoid the strong influence of the initial conditions and periodicity lengths mentioned by several authors, the initial fields should be mostly random and must not include any special structures. Depending on the problem at hand, the periodicity lengths of the grids should not be below the highest values used in this work. In the zones near the wall finer meshes are desirable, if one wants to achieve better spatial resolution of the maximum values of velocity and temperature variations, or if one wants to investigate fluids with other Prandtl numbers.

If it is not possible to refine the grid in order to simulate convection at higher Rayleigh numbers, subgrid-scale structure models should be used. Verifications of these models can only be made by comparison with calculations without subgrid-scale structure models for low Rayleigh numbers, because really comprehensive detailed experimental information, especially for temperature statistics, is missing. The normalization used here allows direct comparison of results involving high and low Rayleigh numbers.

Case	KM	K = 1	2	3	4	5	6	7	8
1–4	8	0·125	0·125	0·125	0·125 c	0·125	0·125	0·125	0·125
5	8	0·0625	0·125	0·125	0·1875 c	0·1875	0·125	0·125	0·0625
6–12	16	0·02	0·03	0·045	0·065	0·08	0·08	0·09	0·09 c

TABLE 4. Distribution of the vertical mesh width Δx_3 over the vertical mesh index K. 'c' marks the centre of the channel with respect to which grids are symmetrical. The grids of cases 13 and 14 are derived from cases 6–12 by halving Δx_3.

Appendix. Influences of the grid

A. 1. *Introduction*

The grids that can be realized on present-day computer systems delimit the accurate description of short-wave events, on the one hand, and long-wave events, on the other. For example the pronounced changes of the vertical temperature gradient near the wall and the smallest vortices, whose scales decrease with increasing Rayleigh number, require very short mesh widths. The large-scale structures observed in many experiments, and the maximum possible wavelength of the roll vortices, according to stability analysis, depend on the length of periodicity included in the simulation. The influence of both constraints will be discussed below using the example of the results of cases 4–14. The high-resolution cases 12–14 are discussed in more detail in Grötzbach (1980).

A. 2. *Limited simulation of minimum wavelengths*

A. 2.1. *Influence of mesh-width distribution in the vertical direction.* Three different grids are used at $Ra = 87\,300$, cases 4–6, which differ most strongly in the vertical mesh width Δx_3 in the zone near the wall ($K = 1, 2$ and $K = KM - 1, KM$) (table 4). The Nusselt number (table 2) shows a non-uniform tendency towards lower values with increasing resolution in the zone near the wall. Figure 8 clearly shows the maximum value (for case 4) to be too high. Obviously Δx_{3w} is not sufficient to resolve adequately the temperature gradient at the wall. The comparison of the three related vertical temperature profiles in figure 15 shows comparable results for cases 5 and 6 only.

The r.m.s. values of the velocity fluctuations (figure 11 and table 2) do not show distinct tendencies. By contrast, the r.m.s. temperature values exhibit an increasing tendency with increasing resolution. In case of really insufficient spatial resolution it should decrease; see below. This is due to volume integration according to (2), which implies that the peak of the r.m.s. value profile, which is closely limited in space, is flattened with increasing mesh widths (figure 15). Thus, if the results are interpreted correctly, the apparent rise does not indicate a lack of simulation. (The slight decrease of r.m.s. temperature values to the next higher Rayleigh number in figure 12 is also attributable to volume averaging because of the smaller spatial extension of the peak.)

A. 2.2. *Influence of mesh width in the horizontal direction.* The influence of horizontal mesh widths can be investigated for cases 7, 9, 12 and 13, 14 at $Ra = 381\,225$. In each case, approximately the same periodicity lengths $X_{1,2}$ have been used by successively halving one of the mesh widths Δx_i (table 1). In cases 12–14, where resolution is better, the flow structures appearing in the contour line plots (figure 16) are comparable qualitatively with those of case 9 (figure 7); the only difference being that the isolines
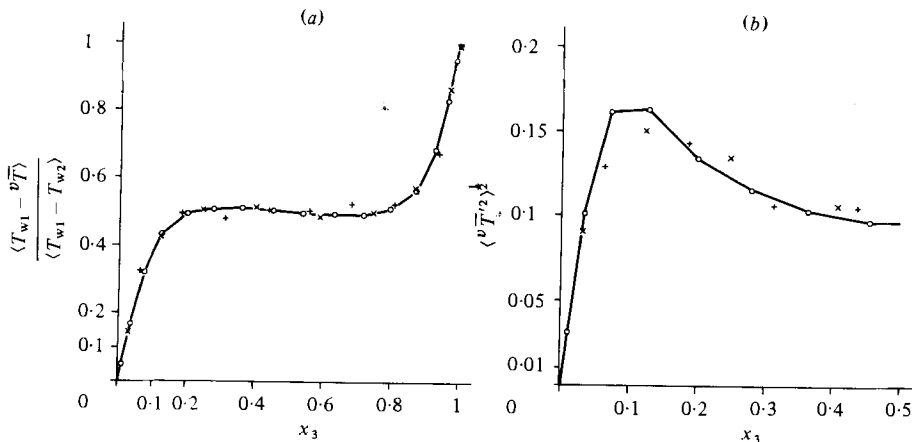
FIGURE 15. Influence on the vertical temperature (a) and r.m.s. temperature value (b) profiles at $Ra = 87\,300$ of the vertical mesh widths Δx_{3w} next to the wall. $+$, $\Delta x_{3w} = 0.125$; $\times$, 0.0625; $\bigcirc$, 0.02.

are smoother owing to the larger number of mesh cells. As to quantitative results, the Nusselt number is about 10% lower than in case 7 and 6% lower than in case 9 (table 5). It can be seen from figure 8 that the lowest numerical results come close to the experimental data, but that the deviations are still about 10%.

In all of the high-resolution cases averaging was done over a larger number NM of time steps (table 1). Nevertheless, statistical evidence of these average values is still limited, as can be seen from the standard deviations of the results given in table 5. The r.m.s. values of the velocity fluctuations scatter considerably, but show no distinct dependency on grid mesh widths. The r.m.s. temperature values seem to show a non-uniform, slightly decreasing tendency with increasing resolution, but the results of cases 9 and 14, for example, differ by less than 4%. Thus, we may conclude that the grid in cases 7 and 8 has an insufficient spatial resolution. The grid in case 9 comes close to the limit of resolution. It leads to uncertainties of, typically, only 6%.

A. 3. *Limited simulation of maximum wavelengths*

A. 3.1. *Influence of the periodicity length.* The periodicity lengths X_1 and X_2 should be prescribed at such high values that the events in the centre of the channel volume considered are not coupled statistically to the events at the boundaries. The extent to which the periodicity length $X_1 = 2.8$, which is used mostly, influences the results can be evaluated by comparison of cases 7–9 with $Ra = 381\,225$ (tables 1 and 2). Cases 7 and 8 differ only in the mesh number IM in the x_1 direction, and thus by a factor of 2 in periodicity lengths $X_1 = IM\,\Delta x_1$.

Qualitative comparison of some isoline and vector plots for case 8 with the greatest periodicity length (figure 17) and the plots for case 9 (figure 7) leads to comparable dimensions for the structures. No large-scale structures are formed in case 8. The quantitative comparison of cases 7 and 8 in table 2 does not reveal any influence. The Nusselt number remains unaffected by X_1, like the relatively highly scattering r.m.s. values of the velocity and temperature fluctuations.

A. 3.2. *Influence of three-dimensionality.* Problems were mentioned in §1 which above all occur in two-dimensional simulation, such as the tendency towards higher
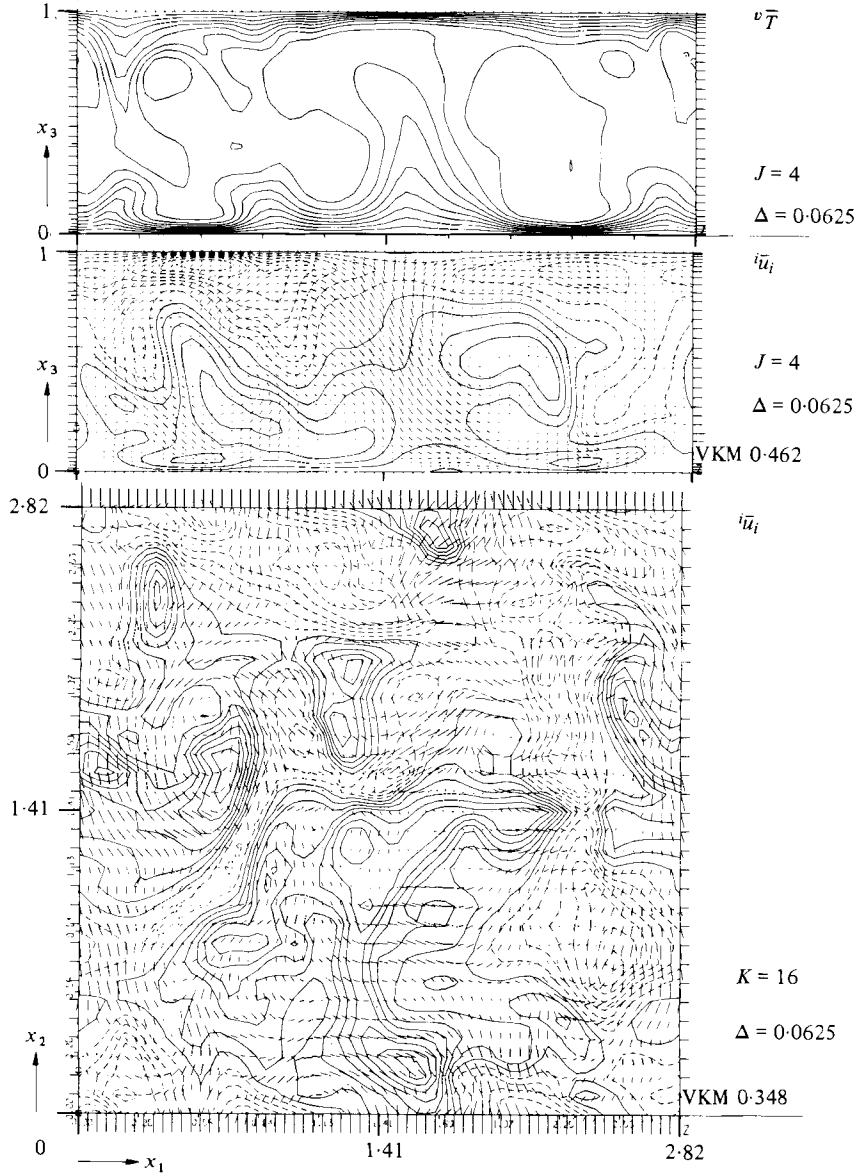
FIGURE 16. Vertical and horizontal sections of the temperature and velocity fields at $t = 32.75$ for $Ra = 381225$, case 14, (x_1, x_3)-plane and (x_1, x_2)-plane.

Case	$\bar{h}$	Nu	$(\langle {}^1\bar{u}_1'^2 \rangle_{\text{max}})^{\frac{1}{2}}$	$(\langle {}^2\bar{u}_2'^2 \rangle_{\text{max}})^{\frac{1}{2}}$	$(\langle {}^3\bar{u}_3'^2 \rangle_{\text{max}})^{\frac{1}{2}}$	$(\langle {}^v\bar{T}'^2 \rangle_{\text{max}})^{\frac{1}{2}}$
7	0.1242	7.75 ± 0.35	0.163 ± 0.010	0.180 ± 0.018	0.207 ± 0.012	0.166 ± 0.007
9	0.0987	7.44 ± 0.29	0.151 ± 0.008	0.163 ± 0.016	0.207 ± 0.009	0.157 ± 0.006
12	0.0785	6.80 ± 0.26	0.202 ± 0.014	0.162 ± 0.010	0.199 ± 0.005	0.159 ± 0.005
13	0.0623	7.04 ± 0.30	0.166 ± 0.008	0.170 ± 0.012	0.203 ± 0.012	0.152 ± 0.004
14	0.0495	6.93 ± 0.16	0.166 ± 0.010	0.170 ± 0.009	0.214 ± 0.011	0.151 ± 0.005

TABLE 5. Influence of the mean grid width $\bar{h} = (\Delta x_1 \Delta x_2 \overline{\Delta x_3})^{\frac{1}{3}}$ $(\overline{\Delta x_3} = 1/KM)$ on the Nusselt number and maximum r.m.s. values of velocity and temperature fluctuations at $Ra = 381225$
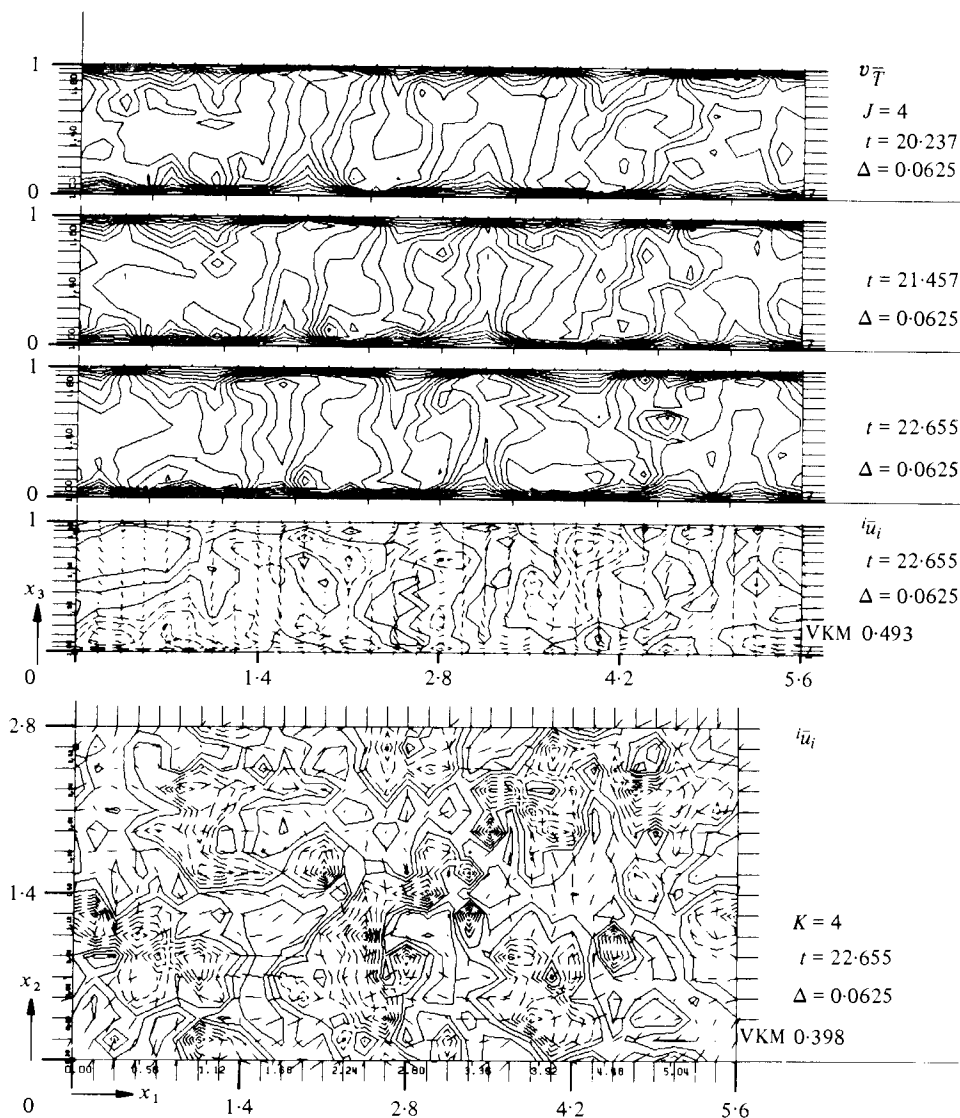
FIGURE 17. Vertical and horizontal sections of the temperature and velocity fields at different times for $Ra = 381\,225$, case 8, (x_1, x_3)-plane and (x_1, x_2)-plane.

Nusselt numbers and shorter wavelengths. From the results of cases 10 and 11 it appears that an analogous experience with TURBIT can be made in two-dimensional simulation. Two-dimensional simulations are approximated here by a reduction to $JM = 2$ (table 1), which results in stronger statistical coupling in the x_2 direction. In periodicity lengths X_1 these cases correspond to cases 7 and 8.

In quantitative comparison of the numerical results for cases 10 and 11 the periodicity length X_1 exerts practically no visible influence (table 2). By contrast, both cases differ quite remarkably from the three-dimensional simulations 7 and 8. The characteristic vortex dimension λ (table 3) is much smaller in the two-dimensional case, although much larger vortices could develop because of the greater periodicity length.

This was also observed by Lipps & Somerville (1971) in pure two-dimensional simulations. The Nusselt numbers are much too high (see table 2 and figure 8). According to Lipps & Somerville (1971) the Nusselt number can only be improved by forced fitting of λ.

The r.m.s. values of the temperature fluctuations do not undergo any modification (table 2). Consequently the buoyancy term in the momentum equation remains unchanged. Since the velocity fluctuations in the x_2 direction are strongly attenuated, owing to the short periodicity length $X_2 = JM \Delta x_2 = 0.35$, the turbulence energy is distributed essentially among the u_1 and u_3 components only. Therefore the turbulence-energy profiles (half the sum of squares of the r.m.s. values) differ by only 10 % at the maximum, although the u_1 and u_3 r.m.s. values are too high (figure 11). The vertical heat-flux cross-correlation coefficients (table 2) are unchanged. They lie in a realistic range, despite erroneous u_3 r.m.s. values. The reason is that the Nusselt number as a measure of the dominant turbulent heat flux is too high by approximately the same factor as the u_3 r.m.s. value.

A. 4. *Conclusions from the influences of the grid*

Investigation of the limited resolution for short wavelengths of the grids led to the following results. Assignment to the Rayleigh numbers of the vertical mesh division selected was considered appropriate. Only two exceptions were found. Firstly for the vertical division of the grid of case 4, which created equidistant meshes, the slightly high Nusselt number and the temperature profile indicate an insufficient resolution of the vertical temperature gradients at the walls. Secondly, halving the horizontal mesh width at the maximum Rayleigh number produced a minor quantitative influence on the general grid resolution capability. From several results of cases 12–14 the conclusion can be drawn that the grid of case 9 comes close to the limit of resolution for the smallest vortices occurring. Thus cases 7 and 8 have insufficient spatial resolutions. At higher Rayleigh numbers subgrid-scale structure models will be necessary with most of the grids used here. The theory of calculating the coefficients of the subgrid-scale heat-flux model available in the TURBIT-3 code has been proven to be a proper tool for assessing the spatial resolution capabilities of the grid chosen (Grötzbach 1980).

The limited resolution for high wavelengths had no special effect. It was reflected quantitatively only in small characteristic vortex dimensions and correlation lengths, respectively. Thus the periodicity length seems to have a similar influence on the characteristic wavelength as the aspect ratio in finite channels, because Fitzjarrald (1976) also found decreasing dominant wavelengths with increasing Ra in low-aspect-ratio experiments. Effects on other statistical data of the turbulence fields at high Rayleigh numbers do not appear. Experience accumulated by other authors is reproduced here in approximately two-dimensional simulations, for example the tendency towards higher Nusselt numbers and shorter wavelengths. Thus the insensitivity to grid parameters observed in the other cases is a physical result reproduced correctly by the computer program.

REFERENCES

ADRIAN, R. J. 1975 Turbulent convection in water over ice. *J. Fluid Mech.* **69**, 753–781.

BROWN, W. 1973 Heat-flux transitions at low Rayleigh number. *J. Fluid Mech.* **60**, 539–559.

BUSSE, F. H. & CLEVER, R. M. 1979 Instabilities of convection rolls in a fluid of moderate Prandtl number. *J. Fluid Mech.* **91**, 319–335.

BUSSE, F. H. & WHITEHEAD, J. A. 1974 Oscillatory and collective instabilities in large Prandtl number convection. *J. Fluid Mech.* **66**, 67–79.

CHU, T. Y. & GOLDSTEIN, R. J. 1973 Turbulent convection in a horizontal layer of water. *J. Fluid Mech.* **60**, 141–159.

CLEVER, R. M. & BUSSE, F. H. 1978 Large wavelength convection rolls in low Prandtl number fluids. *Z. angew. Math. Phys.* **29**, 711–714.

DALY, B. J. 1974 A numerical study of turbulence transitions in convective flow. *J. Fluid Mech.* **64**, 129–165.

DEARDORFF, J. W. & WILLIS, G. E. 1965 The effect of two-dimensionality on the suppression of thermal turbulence. *J. Fluid Mech.* **23**, 337–353.

DEARDOFF, J. W. & WILLIS, G. E. 1967 Investigation of turbulent thermal convection between horizontal plates. *J. Fluid Mech.* **28**, 675–704.

DENTON, R. A. & WOOD, I. R. 1979 Turbulent convection between two horizontal plates. *Int. J. Heat Mass Transfer* **22**, 1339–1346.

DUBOIS, M. & BERGÉ, P. 1978 Experimental study of the velocity field in Rayleigh–Bénard convection. *J. Fluid Mech.* **85**, 641–653.

FITZJARRALD, D. E. 1976 An experimental study of turbulent convection in air. *J. Fluid Mech.* **73**, 693–719.

GILLE, J. 1967 Interferometric measurement of temperature gradient reversal in a layer of convecting air. *J. Fluid Mech.* **30**, 371–384.

GOLDSTEIN, R. J. & CHU, T. Y. 1969 Thermal convection in a horizontal layer of air. *Prog. Heat Mass Transfer* **2**, 55–75.

GRÖTZBACH, G. 1977 Direkte numerische Simulation turbulenter Geschwindigkeits-, Druck- und Temperaturfelder bei Kanalströmungen. KfK 2426, Thesis, Universität Karlsruhe. (English translation in DOE-tr-61.)

GRÖTZBACH, G. 1979 Numerical investigation of radial mixing capabilities in strongly buoyancy-influenced vertical, turbulent channel flows. *Nucl. Engng & Design* **54**, 49–66.

GRÖTZBACH, G. 1980 Über das räumliche Auflösungsvermögen numerischer Simulationen von turbulenter Bénard-Konvektion. KfK 2981 B.

GRÖTZBACH, G. & SCHUMANN, U. 1979 Direct numerical simulation of turbulent velocity-, pressure- and temperature-fields in channel flows. In *Turbulent Shear Flows I* (ed. F. Durst, B. E. Launder, F. W. Schmidt & J. H. Whitelaw), pp. 370–385. Springer.

HOLLANDS, K. G. T., RAITHBY, G. D. & KONICEK, L. 1975 Correlation equations for free convection heat transfer in horizontal layers of air and water. *Int. J. Heat. Mass Transfer* **18**, 879–884.

KOSCHMIEDER, E. L. & PALLAS, S. G. 1974 Heat transfer through a shallow, horizontal convecting fluid layer. *Int. J. Heat Mass Transfer* **17**, 991–1002.

KRISHNAMURTI, R. 1970 On the transition to turbulent convection. Part 1. The transition from two- to three-dimensional flow. *J. Fluid Mech.* **42**, 295–307.

KRISHNAMURTI, R. 1973 Some further studies on the transition to turbulent convection. *J. Fluid Mech.* **60**, 285–303.

LIPPS, F. B. 1976 Numerical simulation of three-dimensional Bénard convection in air. *J. Fluid Mech.* **75**, 113–148.

LIPPS, F. B. & SOMERVILLE, C. J. 1971 Dynamics of variable wavelength in finite-amplitude Bénard convection. *Phys. Fluids* **14**, 759–765.

MALKUS, W. V. R. 1954 Discrete transitions in turbulent convection. *Proc. R. Soc. Lond.* A **225**, 185–195.

OZOE, H., YAMAMOTO, K., CHURCHILL, S. W. & SAYAMA, H. 1976 Three-dimensional, numerical analysis of laminar natural convection in a confined fluid heated from below. *J. Heat Transfer* **98**, 202–207.

SCHUMANN, U. 1973 Ein Verfahren zur direkten numerischen Simulation turbulenter Strömungen in Platten- und Ringspaltkanälen und über seine Anwendung zur Untersuchung von Turbulenzmodellen. KfK 1854, Thesis, Universität Karlsruhe.

SCHUMANN, U. 1975a Subgrid scale model for finite difference simulations of turbulent flows in plane channels and annuli. *J. Comp. Phys.* **18**, 376–404.

SCHUMANN, U. 1975*b* Linear stability of finite difference equations for three-dimensional flow problems. *J. Comp. Phys.* **18**, 465–470.

SILVESTON, P. L. 1958 Wärmedurchgang in waagerechten Flüssigkeitsschichten. *Forsch. Ing.-Wes.* **24**, 29–32, 59–69.

THOMAS, D. B. & TOWNSEND, A. A. 1957 Turbulent convection over a heated horizontal surface. *J. Fluid Mech.* **2**, 473–492.

THRELFALL, D. C. 1975 Free convection in low-temperature gaseous helium. *J. Fluid Mech.* **67**, 17–28.

WILLIS, G. E. & DEARDORFF, J. W. 1965 Measurements on the development of thermal turbulence in air between horizontal plates. *Phys. Fluids* **8**, 2225–2229.

WILLIS, G. E., DEARDORFF, J. W. & SOMERVILLE, R. C. J. 1972 Roll-diameter dependence in Rayleigh convection and its effect upon the heat flux. *J. Fluid Mech.* **54**, 351–367.